arXiv:1602.03566v1 [cond-mat.mes-hall] 10 Feb 2016

Inversion-symmetry-breaking-activated shear Raman bands in T'-$MoTe_2$

Shao-Yu Chen[1], Thomas Goldstein[1], Ashwin Ramasubramaniam[2], and Jun Yan[1*]
[1] *Department of Physics, University of Massachusetts, Amherst, MA 01003, USA*
[2] *Department of Mechanical & Industrial Engineering, University of Massachusetts, Amherst, MA 01003, USA*

(Dated: February 12, 2016)

Type-II Weyl fermion nodes, located at the touching points between electron and hole pockets, have been recently predicted to occur in distorted octahedral (T') transition metal dichalcogenide semimetals, contingent upon the condition that the layered crystal has the noncentrosymmetric orthorhombic (T'_{or}) stacking. Here, we report on the emergence of two shear Raman bands activated by inversion symmetry breaking in T'-$MoTe_2$ due to sample cooling. Polarization and crystal orientation resolved measurements further point to a phase transition from the monoclinic (T'_{mo}) structure to the desired T'_{or} lattice. These results provide spectroscopic evidence that low-temperature T'-$MoTe_2$ is suitable for probing type-II Weyl physics.

PACS numbers: 78.30.-j, 61.50.Ah, 61.50.Ks

T' transition-metal dichalocgenides (T'-TMDCs), in which the metal atoms are octahedrally coordinated and subject to a Peierls-like metal-metal zigzag bonding distortion, are emerging as a class of materials with intriguing non-trivial band topology. Monolayer T'-TMDCs have been shown theoretically to be two dimensional topological insulators [1] whereas bulk T'-TMDCs with appropriate layer stacking are predicted to be type-II Weyl semimetals [2]. Originally a fundamental high-energy-physics concept in quantum field theory [3], Weyl fermions have recently been proposed and demonstrated as a new type of condensed matter quasi-particle excitation [4–11]. In these solid state systems, paired Weyl nodes are located at distinct positions in the crystal momentum space with each node acting as a 'magnetic monopole' from which Berry flux emanates in directions determined by the node's chirality. This leads to anomalous phenomena including Fermi arcs on separate crystal surfaces connected through the bulk [12], and apparent violation of charge conservation for electrons with a definite chirality propagating in parallel electric and magnetic fields [13].

Depending upon the material-specific Fermi velocity tensor, the Weyl nodes can either appear as a point-like Fermi surface (type-I) or as the touching points between electron and hole pockets (type-II)[2]. Type-I Weyl nodes have been demonstrated in recent experimental studies of TaAs [6–9], NbAs [10] and TaP [11], while type-II Weyl nodes, a more recent theoretical development [2], remains to be confirmed experimentally. Distorted octahedral orthorhombic (T'_{or}) WTe_2 was the first material predicted to be a type-II Weyl semimetal [2]. Subsequent theoretical investigations showed that the T'_{or} phase of $MoTe_2$ also possess type-II Weyl nodes [14]. Numerical calculations reveal that T'_{or}-$MoTe_2$ has much larger Weyl-node-pair separations than WTe_2 [2, 14]. Closely-spaced Weyl nodes may become more vulnerable to internode scattering, and lead to short Fermi arcs, making it more challenging to investigate with tools such as angle-resolved photo emission spectroscopy. This makes T'_{or}-$MoTe_2$ potentially a more promising candidate for investigating the quantum behavior of Weyl fermions.

However, unlike WTe_2 that has the desired T'_{or} phase for Weyl nodes, semimetallic $MoTe_2$ crystallizes in the undesirable monoclinic (T'_{mo}) phase (also called β-$MoTe_2$) at room temperature [15]; a recent study further indicates that this T'_{mo} phase prevails in T'-$MoTe_2$ down to 1.8 Kelvin [16], while earlier investigations suggested that the low temperature structure might be altogether different [17, 18]. The T'_{mo} lattice has both time-reversal symmetry and inversion symmetry, making it impossible to have the topologically non-trivial electronic bands for a Weyl semimetal. This undesired T'_{mo} phase, in fact, prompted the investigation of $Mo_xW_{1-x}Te_2$ that inherits the T'_{or} structure of WTe_2 and enables large Weyl-node-pair separations [19, 20]. From an experimental point of view, $MoTe_2$ is a stoichiometric compound and would be preferred over $Mo_xW_{1-x}Te_2$ for investigating Weyl physics provided that its T'_{or} phase can be established rigorously. Presently, the existence of orthorhombic T'-$MoTe_2$ is being debated [14, 19–21] and more experimental studies are needed to elucidate the low-temperature phase of the crystal.

In this Letter, we make use of Raman scattering to systematically monitor the inversion symmetry and the crystal phase of T'-$MoTe_2$ as a function of temperature. At low temperatures, two low-energy modes (at 12.6 and 29.1 cm^{-1} respectively) associated with interlayer shear vibrations, one perpendicular and the other parallel to the distorted zigzag metal chains, appear in the spectra. We conclude from symmetry analysis that the appearance of the two Raman bands is a consequence of inversion symmetry breaking. The thermal cycling as well as the polarization-resolved and crystal-orientation-resolved Raman tensor analysis further confirm that during cooling, a structural phase transtion from T'_{mo} to T'_{or}

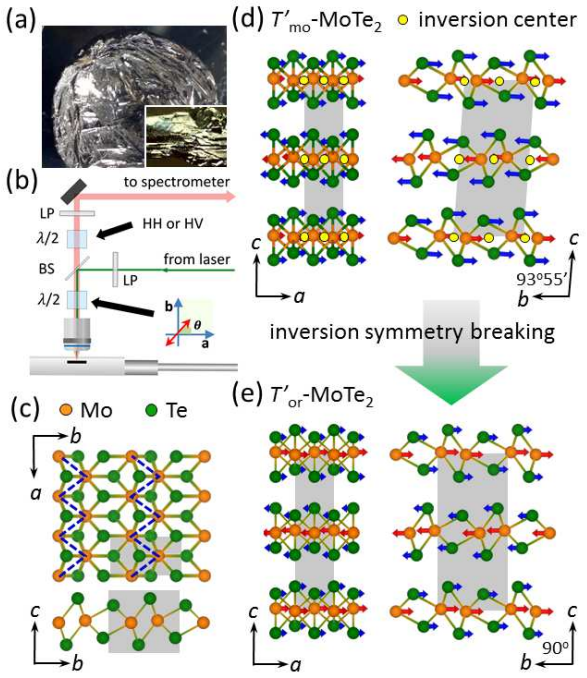

FIG. 1. (a) Pictures of bulk T'-$MoTe_2$. Inset is a zoom-in for showing detailed sample morphology. (b) Schematic of polarization-resolved and crystal-orientation-resolved Raman spectroscopy. (c) The top view (a-b plane) and side view (b-c plane) of monolayer T'-$MoTe_2$. The blue dashed lines indicate the Mo-Mo zigzag chain which is aligned with the a-axis. (d)&(e) The shear vibrations in T'_{mo} (d) and T'_{or} (e) $MoTe_2$. (left: shear mode along a-axis; right: shear mode along b-axis). The shaded areas in (c)-(e) show the unit cell of T'-$MoTe_2$ in the corresponding phases. The inversion symmetry is broken in T'_{or}-$MoTe_2$.

has occurred. These findings provide strong evidence for the low temperature Weyl T'_{or} phase of the semimetallic $MoTe_2$. Furthermore, our experiments offer insights into inversion symmetry breaking in T'-$MoTe_2$ that can be of significance to nonlinear optics [22, 23], and open up a venue for investigating stacking dependent vibrational, optical and electronic properties of T'-$MoTe_2$ atomic layers.

The T'-$MoTe_2$ crystal used in this work is grown by chemical vapor transport method using Bromine as the transport agent. At room temperature the most stable phase of $MoTe_2$ is the hexagonal semiconducting phase (also called α-$MoTe_2$). To crystalize in the metastable semimetallic phase we thermally quench the crystal from 900 °C to room temperature with water bath. The image of a typical crystal is shown in Fig.1(a). The crystal shows layered structure and needle-like shape with lengths ranging from a few mm to 1 cm.

Figure 1(b) schematically shows our experimental setup. The T'-$MoTe_2$ crystals are mounted in a microscopy cryostat with the flat plane facing up. Linearly polarized light from a frequency doubled Nd:YAG laser at 532 nm is used to excited the sample in back-scattering geometry. We place a half waveplate between the beam splitter (BS) and the microscope objective to adjust the angle θ of the incident light polarization direction with respect to the crystal a-axis. Another half waveplate is mounted in the collection path after the beam splitter followed by a linear polarizer (LP) so that we can selectively collect the scattered light that is polarized either parallel (HH) or perpendicular (HV) to the incident beam. The scattered light is then dispersed by Horiba T64000 triple spectrometer operating in subtractive mode, and detected by a liquid nitrogen cooled CCD camera.

Figure 1(c) shows the top and side views of the atomic arrangements in a T'-$MoTe_2$ monolayer. The in-plane a and b axes are parallel and perpendicular to the zigzag Mo-Mo chains respectively. In bulk crystals, the neighboring $MoTe_2$ layers are rotated from one another by 180° about an axis perpendicular to the atomic layer. This results in two $MoTe_2$ layers per bulk unit cell, as enclosed by the shaded parallelogram and rectangles in Figs.1 (d)&(e). Consequently both T'_{mo} and T'_{or} structures support shear mode vibrations as illustrated by the arrows in the drawings. We note that due to in-plane anisotropy in T' crystals, the shear mode vibrations along the a and b axes are non-degenerate, in contrast to the hexagonal phase [24–26].

The T'_{mo} and T'_{or} phases differ in their c-axis directions: in the former the c-axis makes an angle of 93°55′ with the b-axis, whereas in the latter the c-axis is perpendicular to the atomic plane. While differing only by a small shift of the atomic layers along the b-axis direction, the two phases have important differences in symmetry. In particular, T'_{mo} is inversion symmetric (inversion centers are noted as yellow dots in Fig.1(d)) while T'_{or} is non-centrosymmetric. This inversion symmetry is the key reason why T'_{mo}-$MoTe_2$ can not be a Weyl semimetal [14], and the breaking of this symmetry is a focus of this paper.

Figure 2(a) shows typical Raman spectra of T'-$MoTe_2$, collected as the crystal is cooled down from 286 K to 80 K and warmed back up to 286 K, with incident and scattered light linearly polarized perpendicular to each other (HV), and making a 45° angle with the a-axis of the crystal. Because of the relatively large number of atoms (12) in the T' unit cell as compared to the hexagonal phase, the spectra display many first order phonon bands below 300 cm^{-1}. In this paper we will focus on the low wavenumber regime (Fig.2(b)) wherein the symmetry-breaking between the T'_{or} and T'_{mo} phases is readily discerned; systematic analysis of the high-energy optical phonons will be presented elsewhere. As seen in Fig. 2(a), cooling induces a new Raman peak S_1 at 12.6 cm^{-1} in the spectrum and it persists when the sample is warmed back up. In Fig.2(b), we also display spectra with the incident and scattered light linearly po-

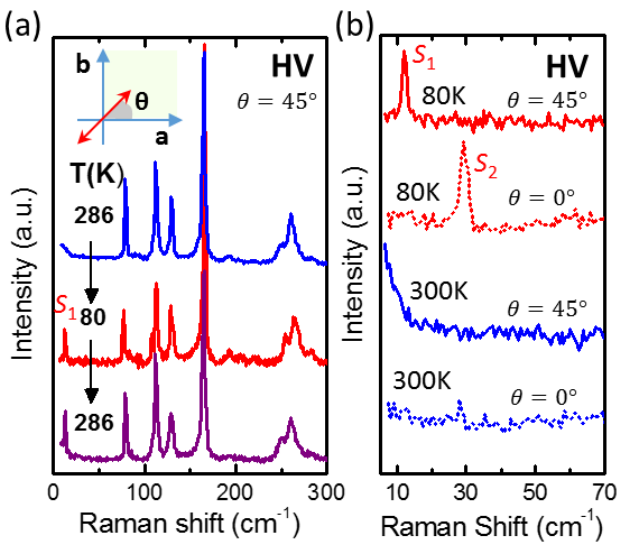

FIG. 2. (a) The Raman spectra of T'-$MoTe_2$ under different thermal cycles. The low wavenumber shear mode (S_1) emerges when cooling down from 286 K (blue) to 80 K (red) and persists during warming up to 286 K (purple). (b) The Raman spectra of low wavenumber modes of T'-$MoTe_2$ at 80 K and 300 K at different crystal orientation angles. The spectra in both figures are taken in the HV configuration.

larized along the a and b axes respectively (HV, θ=0°). In this detection configuration, we observe another new Raman band S_2 at 29.1 cm^{-1} at low temperature.

To understand the origin of these new vibrational features, we performed lattice dynamics calculations using plane-wave density functional theory (DFT) as implemented in the Vienna Ab Initio Simulation Package (VASP)[27, 28]. As standard DFT functionals fail to describe interlayer van der Waals bonding correctly, we used the non-local optB86b van der Waals functional[29, 30], which reproduces the equilibrium geometry of $MoTe_2$ accurately[31]. By scrutinizing the normal modes from our DFT calculations, we find that in the T'_{mo} phase the shear modes along the b and a axes are at 9.2 cm^{-1} and 27.2 cm^{-1}, respectively, whereas in T'_{or} phase the two modes are found at 15.3 and 29.3 cm^{-1}. Therefore, we attribute the experimentally observed low-energy S_1 and S_2 peaks in Fig.2 to the interlayer shear modes along the b and a axes respectively.

Because both T'_{mo} and T'_{or} phases host these shear vibrations as illustrated in Fig.1(d)&(e) and confirmed by the DFT calculation, it is not obvious to which crystal phase the Raman peaks in Fig.2 belong. Raman intensity of materials can have unusual temperature dependencies [32]. Could it be that the crystal is in the same T'_{mo} phase at all temperatures, and that its shear modes somehow only have observable Raman intensity at low temperature? The data in Fig.2(a) suggest that this is not the case: S_1 is absent in the original warm sample at 286 K, shows up at 80 K, and persists as the sample is warmed back up to 286 K. The significant hysteresis (more details in Fig.4) indicates that the appearance of S_1 and S_2 are due to structural, instead of thermal reasons, i.e., at the same temperature the shear modes may or may not appear depending on the underlying crystal structure.

The reason why S_1 and S_2 do not appear in T'_{mo}-$MoTe_2$ Raman spectra can be understood from symmetry. The inversion centers of the monoclinic structure (Fig.1(d) yellow dots) are located within the $MoTe_2$ layer. As a result, S_1 and S_2 vibrations change their directions under inversion. These odd shear modes are thus infrared (IR) active. IR and Raman active modes in centrosymmetric crystals are mutually exclusive, which explains the absence of S_1 and S_2 in Raman spectra of T'_{mo}-$MoTe_2$ in Fig.2. This is in contrast to, say, hexagonal bilayer TMDCs, whose inversion centers are located between the TMDC layers, and which, consequently, have even shear modes that are Raman active[24–26]. The appearance of S_1 and S_2 Raman bands due to sample cooling thus presents a signature for inversion symmetry breaking, which incidentally and importantly, is also a necessary (albeit not sufficient) condition for the existence of Weyl fermions in a non-magnetic material.

To further establish that the two low-energy Raman peaks are indeed linked to the Weyl T'_{or}-$MoTe_2$ phase, we perform polarization and crystal-orientation resolved Raman tensor analysis. The T'_{or}-TMDC structure has three symmetry operations including a mirror plane (m), a glide plane (n) and a two-fold screw axis (2_1) that form the C^7_{2v} group (No. 31 $Pmn2_1$ space group)[15]. Performing these operations explicitly upon the atomic displacements in Figs.1(d)&(e), we found that S_1 along the b axis is symmetric under all three operations, while S_2 along the a axis is symmetric under 2_1 and antisymmetric under the other two operations. Hence S_1 is expected to have A_1 symmetry and S_2 should be A_2.

The Raman tensor $\mathcal{R}$ for the A_1 and A_2 modes of C_{2v} point group are given respectively by [33]:

$$\mathcal{R}(A_1) = \begin{pmatrix} d & 0 & 0 \\ 0 & e & 0 \\ 0 & 0 & f \end{pmatrix}, \mathcal{R}(A_2) = \begin{pmatrix} 0 & g & 0 \\ g & 0 & 0 \\ 0 & 0 & 0 \end{pmatrix}. \quad (1)$$

The Raman cross-section is expressed as $\mathcal{I} = | < \epsilon_i|\mathcal{R}|\epsilon_o > |^2$, where ϵ_i and ϵ_o are polarization states of the incident and scattered light. Consider backscattering geometry using linearly polarized light with $\epsilon_i = (\cos\theta, \sin\theta, 0)$ and $\epsilon_o = (\cos\phi, \sin\phi, 0)$, where θ and ϕ are angles between the direction of $MoTe_2$ crystal a-axis and that of the light polarization. The Raman cross sections for A_1 and A_2 are:

$$\mathcal{I}(A_1) = (d\cos\theta\cos\phi + e\sin\theta\sin\phi)^2,$$
$$\mathcal{I}(A_2) = (g\sin(\theta+\phi))^2. \quad (2)$$

In our measurement, HH configuration corresponds to

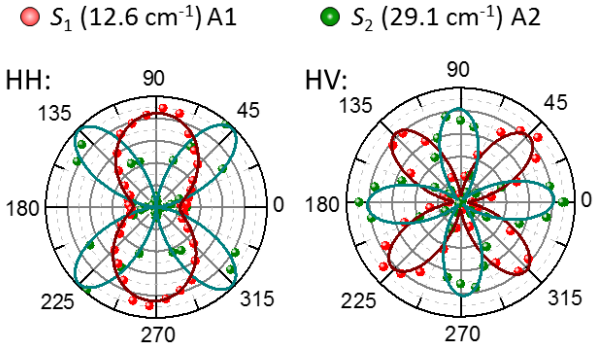

FIG. 3. Polarization (HH or HV configuration) and crystal orientation dependent intensity of shear modes, S_1 (red) and S_2 (green). The solid curves are fits using equation (3) in the text. The numbers on the angular axis indicate the angle relative to the a-axis of crystal, as denoted by θ in Fig.2.

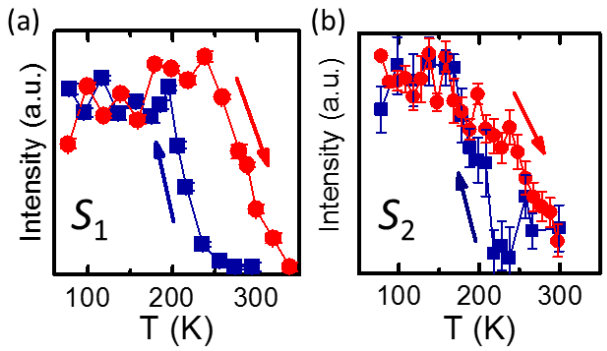

FIG. 4. Temperature dependent intensity of shear modes. (a)S_1 and (b)S_2 under different thermal cycle, cooling (blue) and warming (red). The hysteresis means that both T'_{mo} and T'_{or} phases can coexist in certain temperature range. For temperatures lower than 150 K, the intensity overlaps for cooling and heating, indicating a complete phase transition from T'_{mo} to T'_{or}.

$\phi = \theta$, and HV corresponds to $\phi = \theta + \frac{\pi}{2}$ in Eq.(2). This gives

$$\begin{aligned} \mathcal{I}_{HH}(S_1) &= \left(d\cos^2\theta + e\sin^2\theta\right)^2, \\ \mathcal{I}_{HV}(S_1) &= \left(\frac{d-e}{2}\right)^2 \sin^2(2\theta), \\ \mathcal{I}_{HH}(S_2) &= g^2\sin^2(2\theta), \\ \mathcal{I}_{HV}(S_2) &= g^2\cos^2(2\theta). \end{aligned} \tag{3}$$

Figure 3 presents the angular dependence of the Raman intensities as well as the fits according to Equation (3). In HH configuration, the S_1 mode shows two-fold symmetry while S_2 mode shows four-fold symmetry. In contrast, both S_1 and S_2 exhibit four-fold symmetry albeit with 45° shift in HV scattering geometry. The excellent agreement between data and theoretical calculation verifies the symmetry properties of the two shear modes, and confirms that the observed S_1 and S_2 Raman bands are from the T'_{or} phase of the $MoTe_2$ crystal.

To gain more insight into the inversion-symmetry-breaking phase transition from T'_{mo} to T'_{or}, we monitor the S_1 and S_2 peaks when the sample is cooled down from room temperature and warmed back up. Figure 4 shows the temperature dependence of the S_1 and S_2 intensities as a function of temperature. As can been seen, the cooling (blue) and warming (red) curves do not overlap over extended range of temperatures. The thermal hysteresis suggests that the T'_{mo} to T'_{or} and T'_{or} to T'_{mo} phase transitions take time to complete and the crystal lattice cannot adjust very quickly from one stacking to another. The intensities of the Raman bands tend to coalesce below 200 K and, moreover, the intensity below 150 K is independent of cooling or warming. This indicates that the crystal is stabilized in the pure T'_{or} phase, without any admixtures from the T'_{mo}, which is important for obtaining high quality T'_{or}-$MoTe_2$ crystal to probe the Weyl physics.

In conclusion, the inversion symmetry and the crystal phase of T'-$MoTe_2$ was probed by Raman scattering. The two new shear modes that we observed and systematically analyzed provide strong evidence for the emergence of the orthorhombic T'-$MoTe_2$ phase upon cooling of the room-temperature monoclinic phase. This investigation opens up promising opportunities to investigate the theoretically predicted and yet to be experimentally confirmed type-II Weyl semimetal. We further anticipate that the cooling-driven inversion-symmetry breaking might also be probed by second harmonic generation [22, 23]. Finally, the thermally-driven stacking changes could also occur in atomically-thin T'-$MoTe_2$, raising interesting questions regarding stacking-dependent vibrational, optical and electronic properties, which are know to display rich physics in, for example, another 2D semimetal graphene [34–36].

Acknowledgements

This work is supported by the University of Massachusetts Amherst and in part by the National Science Foundation Center for Hierarchical Manufacturing (CMMI-1025020). Computing support from the Massachusetts Green High Performance Computing Center is gratefully acknowledged.

* yan@physics.umass.edu

[1] X. Qian, J. Liu, L. Fu, and J. Li, Science **346**, 1344 (2014).
[2] A. A. Soluyanov, D. Gresch, Z. Wang, Q. Wu, M. Troyer, X. Dai, and B. A. Bernevig, Nature **527**, 495 (2015).
[3] H. Weyl, Zeitschrift fr Physik **56**, 330 (1929).
[4] H. Weng, C. Fang, Z. Fang, B. A. Bernevig, and X. Dai, Physical Review X **5**, 011029 (2015).
[5] S.-M. Huang, S.-Y. Xu, I. Belopolski, C.-C. Lee, G. Chang, B. Wang, N. Alidoust, G. Bian, M. Neupane,

C. Zhang, S. Jia, A. Bansil, H. Lin, and M. Z. Hasan, Nature communications **6**, 7373 (2015).
[6] S.-Y. Xu, I. Belopolski, N. Alidoust, M. Neupane, G. Bian, C. Zhang, R. Sankar, G. Chang, Z. Yuan, C.-C. Lee, S.-M. Huang, H. Zheng, J. Ma, D. S. Sanchez, B. Wang, A. Bansil, F. Chou, P. P. Shibayev, H. Lin, S. Jia, and M. Z. Hasan, Science **349**, 613 (2015).
[7] B. Lv, H. Weng, B. Fu, X. Wang, H. Miao, J. Ma, P. Richard, X. Huang, L. Zhao, G. Chen, Z. Fang, X. Dai, T. Qian, and H. Ding, Physical Review X **5**, 031013 (2015).
[8] L. X. Yang, Z. K. Liu, Y. Sun, H. Peng, H. F. Yang, T. Zhang, B. Zhou, Y. Zhang, Y. F. Guo, M. Rahn, D. Prabhakaran, Z. Hussain, S.-K. Mo, C. Felser, B. Yan, and Y. L. Chen, Nature Physics **11**, 728 (2015).
[9] B. Q. Lv, N. Xu, H. M. Weng, J. Z. Ma, P. Richard, X. C. Huang, L. X. Zhao, G. F. Chen, C. E. Matt, F. Bisti, V. N. Strocov, J. Mesot, Z. Fang, X. Dai, T. Qian, M. Shi, and H. Ding, Nature Physics **11**, 724 (2015).
[10] S.-Y. Xu, N. Alidoust, I. Belopolski, Z. Yuan, G. Bian, T.-R. Chang, H. Zheng, V. N. Strocov, D. S. Sanchez, G. Chang, C. Zhang, D. Mou, Y. Wu, L. Huang, C.-C. Lee, S.-M. Huang, B. Wang, A. Bansil, H.-T. Jeng, T. Neupert, A. Kaminski, H. Lin, S. Jia, and M. Zahid Hasan, Nature Physics **11**, 748 (2015).
[11] S.-Y. Xu, I. Belopolski, D. S. Sanchez, C. Zhang, G. Chang, C. Guo, G. Bian, Z. Yuan, H. Lu, T.-R. Chang, P. P. Shibayev, M. L. Prokopovych, N. Alidoust, H. Zheng, C.-C. Lee, S.-M. Huang, R. Sankar, F. Chou, C.-H. Hsu, H.-T. Jeng, A. Bansil, T. Neupert, V. N. Strocov, H. Lin, S. Jia, and M. Z. Hasan, Science Advances **1**, e1501092 (2015).
[12] X. Wan, A. M. Turner, A. Vishwanath, and S. Y. Savrasov, Physical Review B **83**, 205101 (2011).
[13] H. Nielsen and M. Ninomiya, Physics Letters B **130**, 389 (1983).
[14] Y. Sun, S.-C. Wu, M. N. Ali, C. Felser, and B. Yan, Physical Review B **92**, 161107 (2015).
[15] B. E. Brown, Acta Crystallographica **20**, 268 (1966).
[16] D. H. Keum, S. Cho, J. H. Kim, D.-H. Choe, H.-J. Sung, M. Kan, H. Kang, J.-Y. Hwang, S. W. Kim, H. Yang, K. J. Chang, and Y. H. Lee, Nature Physics **11**, 482 (2015).
[17] H. P. Hughes and R. H. Friend, Journal of Physics C: Solid State Physics **11**, L103 (1978).
[18] R. Clarke, E. Marseglia, and H. P. Hughes, Philosophical Magazine Part B **38**, 121 (1978).
[19] T.-R. Chang, S.-Y. Xu, G. Chang, C.-C. Lee, S.-M. Huang, B. Wang, G. Bian, H. Zheng, D. S. Sanchez, I. Belopolski, N. Alidoust, M. Neupane, A. Bansil, H.-T. Jeng, H. Lin, and M. Z. Hasan, arXiv:1508.06723 (2015), arXiv:1508.06723.
[20] I. Belopolski, S.-Y. Xu, Y. Ishida, X. Pan, P. Yu, D. S. Sanchez, M. Neupane, N. Alidoust, G. Chang, T.-R. Chang, Y. Wu, G. Bian, H. Zheng, S.-M. Huang, C.-C. Lee, D. Mou, L. Huang, Y. Song, B. Wang, G. Wang, Y.-W. Yeh, N. Yao, J. Rault, P. Lefevre, F. Bertran, H.-T. Jeng, T. Kondo, A. Kaminski, H. Lin, Z. Liu, F. Song, S. Shin, and M. Z. Hasan, , 24 (2015), arXiv:1512.09099.
[21] Z. Wang, D. Gresch, A. A. Soluyanov, W. Xie, S. Kushwaha, X. Dai, M. Troyer, R. J. Cava, and B. A. Bernevig, (2015), arXiv:1511.07440.
[22] N. Kumar, S. Najmaei, Q. Cui, F. Ceballos, P. M. Ajayan, J. Lou, and H. Zhao, Physical Review B **87**, 161403 (2013).
[23] Y. Li, Y. Rao, K. F. Mak, Y. You, S. Wang, C. R. Dean, and T. F. Heinz, Nano letters **13**, 3329 (2013).
[24] Y. Zhao, X. Luo, H. Li, J. Zhang, P. T. Araujo, C. K. Gan, J. Wu, H. Zhang, S. Y. Quek, M. S. Dresselhaus, and Q. Xiong, Nano letters **13**, 1007 (2013).
[25] S.-Y. Chen, C. Zheng, M. S. Fuhrer, and J. Yan, Nano letters **15**, 2526 (2015).
[26] G. Froehlicher, E. Lorchat, F. Fernique, C. Joshi, A. Molina-Sánchez, L. Wirtz, and S. Berciaud, Nano letters **15**, 6481 (2015).
[27] G. Kresse and J. Furthmüller, Computational Materials Science **6**, 15 (1996).
[28] The projector-augmented wave (PAW) method [37, 38] was used to represent core and valence electrons. The 4p, 5s, and 4d electrons of Mo, and the 5s and 5p electrons of Te were treated as valence. From convergence tests, a plane-wave cutoff of 325 eV was chosen in conjunction with a Γ-centered, $4 \times 8 \times 2$ k-point mesh for Brillouin zone sampling. For relaxation of the primitive cell, electronic wavefunctions were converged to within 10^{-4} eV; cell vectors and atomic positions were optimized with a force tolerance of 10^{-2} eV/Å followed by an additional relaxation of atomic positions alone with a force tolerance of 10^{-3} eV/ Å . Following structural optimization of primitive cells, vibrational frequencies were obtained within the harmonic approximation using the finite-displacement method in Phonopy [39]. A $4 \times 4 \times 1$ supercell and a $1 \times 2 \times 2$ k-point mesh were employed for the T'_{mo} phase, whereas a larger 4×6 supercell was required for the T'_{or} phase with a $1 \times 1 \times 2$ k-point mesh. A tighter convergence criterion of 10^{-6} eV was used for wavefunctions in these vibrational calculations.
[29] J. Klimeš, D. R. Bowler, and A. Michaelides, Physical Review B **83**, 195131 (2011).
[30] M. Dion, H. Rydberg, E. Schröder, D. C. Langreth, and B. I. Lundqvist, Physical Review Letters **92**, 246401 (2004).
[31] T. Björkman, The Journal of chemical physics **141**, 074708 (2014).
[32] C. H. Lui, Z. Ye, C. Keiser, X. Xiao, and R. He, Nano letters **14**, 4615 (2014).
[33] R. Loudon, Advances in Physics **13**, 423 (1964).
[34] L. Zhang, Y. Zhang, J. Camacho, M. Khodas, and I. Zaliznyak, Nature Physics **7**, 953 (2011).
[35] C. H. Lui, Z. Li, K. F. Mak, E. Cappelluti, and T. F. Heinz, Nature Physics **7**, 944 (2011).
[36] W. Bao, L. Jing, J. Velasco, Y. Lee, G. Liu, D. Tran, B. Standley, M. Aykol, S. B. Cronin, D. Smirnov, M. Koshino, E. McCann, M. Bockrath, and C. N. Lau, Nature Physics **7**, 948 (2011).
[37] P. E. Blöchl, Physical Review B **50**, 17953 (1994).
[38] G. Kresse, Physical Review B **59**, 1758 (1999).
[39] A. Togo and I. Tanaka, Scripta Materialia **108**, 1 (2015).